Article

s-Tetrazine-Bridged Photochromic Aromatic Framework Material

Tao Chen, Guangjun Xiao, Zhuo Wang, Jian Zou, Jian Wang, Weibo Hu,* Yahu A. Liu, Hui Yang,* and Ke Wen*
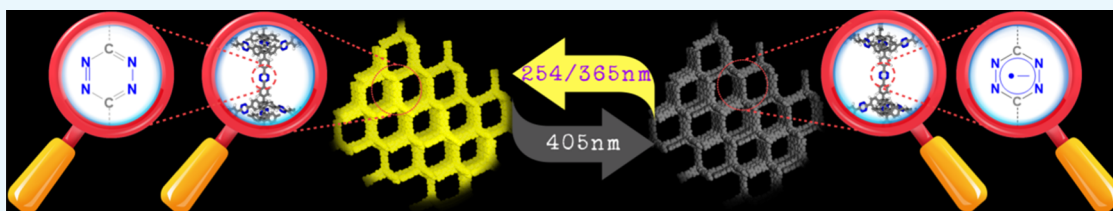
Read Online

ACCESS | Metrics & More | Article Recommendations | Supporting Information

ABSTRACT: Integrating fluorescent chromophores in aromatic frameworks could not only prevent aggregation-induced quenching caused by the $\pi-\pi$ stacking interaction between the chromophore components but also confer new fluorescence properties. Herein, we report the fabrication of s-tetrazine-bridged aromatic frameworks **TzAF** by the incorporation of the smallest aromatic fluorophore, s-tetrazine (**Tz**), into the skeleton of a tetrahedrally connected lattice of aromatic frameworks. The thin films of **TzAF** coated on silica gel plates were found to exhibit reversible photoswitching fluorescence characteristics under alternate UV and visible-light irradiations with excellent fluorescence stability and high on/off contrast. The repeatable "on/off" fluorescence photoswitchability of the **TzAF** thin films was mechanistically attributed to light-induced reversible transformation between **TzAF**'s neutral and radical states.

1. INTRODUCTION

Stimuli-responsive materials are able to reversibly change their physicochemical states and distinguishable properties in response to externally applied stimuli, such as stress, light, temperature, moisture, pH, or electric or magnetic fields.[1−6] For example, photoswitchable fluorescent materials are photochromic fluorophores whose distinct on/off fluorescence emission could be controlled by light.[7−9] As light can be delivered instantly to precise locations of light-responsive materials, such materials have thus found wide application potentials in the areas of information encryption, anticounterfeiting, reversible fluorescence imaging, ultrahigh-resolution bioimaging, photocontrolled biological functions, rewritable printing, and so forth. Photochromic fluorescence materials were usually obtained through a suitable molecular combination of photochromism and fluorescence, that is, chemical association between photochromic and fluorescent molecular components.[7−9] Thus far, various diarylethene (DArE)-based photochromic fluorescent materials have been well reported, thanks to the inherent fluorescence that resulted from resonance energy transfer or intramolecular electron transfer processes possessed by the DArE-based molecular components and their excellent photoswitching properties, biostability, and fatigue resistance.[7−10] Besides DArE, a few other photochromic fluorophores, including the derivatives of spiropyran, spironaphthoxazine, imidazole dimer, dipyrromethene, oxazine, hydrazones, and rhodamine, have also been unveiled.[7−12] Fluorophores emit bright fluorescence in solution, but their

fluorescence intensity is much weaker in the solid states as electronic coupling in well-conjugated and planar aromatic structures quenches fluorescence emission, preventing the reliable translation of fluorescence properties to applications as solid materials.[13,14] To avoid such aggregation-caused quenching (ACQ), fluorophores could be dispersed into lattice porous structures[13] or incorporated as building blocks in the structures of porous solid materials such as metal organic frameworks (MOFs), covalent organic frameworks (COFs),[15] porous organic polymers,[16] or porous aromatic frameworks (PAFs).[17] Toward this end, Laursen, Flood, and co-workers allowed cationic fluorophores cocrystallized into well-defined lattices of ion-sequestering macrocycles to keep the fluorescent dyes from dulling in the solid state.[13] Hill, Ladewig, and co-workers developed photoswitchable fluorescent PAF materials using DArE-based fluorophores as guest molecules.[18] Klajn's group described two families of spiropyran-based fluorescent photoswitchable frameworks in which the spiropyran units were incorporated in the framework skeleton.[17] Zhu's group has developed photoswitchable fluorescent PAF materials by decorating the frame of PAF-5CF with DArE fluorophores.[19]

However, it is challenging to integrate large fluorophores covalently into the aromatic framework skeletons. We envisioned that it could be more straightforward to incorporate covalently smaller photochromic fluorophores into the skeletons. In our search for small non-DArE-based fluorescent photoswitchable materials, we were intrigued by 1,2,4,5-tetrazine (*s*-tetrazine, **Tz**), the arguably smallest and electron-poorest aromatic fluorophore in which the presence of four sp^2 nitrogen atoms makes the ring an exceptionally strong electron acceptor, comparable to tetranitrobenzene.[20−22] With a low-energy $\pi*$ lowest unoccupied molecular orbital (LUMO), the π-aromatic system of **Tz** can be reversibly reduced to a stable radical anion which possesses a distinct different fluorescence property from that of **Tz**.[20,21] For instance, chloromethoxylte-trazine is highly fluorescent in its neutral state, but its radical anion is nonfluorescent.[23,24] Although **Tz** is photochemically unstable, the stability of a substituted **Tz** increases as the size of the substituent(s) increases.[20−22] Therefore, it was reasonable to speculate that incorporating **Tz** units into a PAF skeleton could form a stable porous photochromic fluorescent material. In fact, **Tz** has already been used as a building block in copolymers[25−27] and porous MOFs.[28] Very recently, Ghosh, Abe, Seki, and co-workers stitched **Tz** building blocks into COFs.[29] Nonetheless, **Tz** has not yet been used as a skeleton building unit in PAFs. With previous experience in covalent triazine frameworks (CTFs),[30−32] we therefore embarked on a task of integrating **Tz** units and tetraphenylmethane units to create new aromatic frameworks bearing unique photochromic properties. Herein, we report our work on the development of photoswitchable fluorescent **Tz**-bridged aromatic frameworks (**TzAF**), which demonstrate repeatable "on/off" fluorescence photoswitchability under alternate UV and visible-light irradiation.

2. RESULTS AND DISCUSSION

2.1. Synthetic Procedure. Previously, we have developed a method for the synthesis of CTFs through an aromatic nucleophilic substitution reaction (S$_N$Ar).[30−32] We therefore first tried to synthesize the designed **TzAF** through S$_N$Ar of 3,6-dichloro-1,2,4,5-tetrazine with Grignard reagent **3a** or organolithium reagent **3b** (Scheme 1). Unfortunately, the reaction did not yield the desired product probably due to the poor solubility of organometallic precursors (**3a** and **3b**). Thus, instead of using **Tz**-containing building blocks, we decided to try a de novo synthesis during which dihydro-*s*-tetrazine (dihydro-**Tz**) units were built from nitrile and hydrazine and then oxidized to aromatic **Tz** units. As illustrated in Scheme 1, the attempted reaction of tetrahedral symmetric aromatic nitrile (**4**) and hydrazine catalyzed by sulfur powder yielded the nonconjugated dihydro-**Tz**-bridged cross-linked frames **6**,[33−35] but the sharp heat and gas release of the reaction prompted us to explore a stepwise approach (Figure S7, Supporting Information). Therefore, nitrile **4** was first transformed to amidine **5**, which then reacted with hydrazine to furnish the dihydro-**Tz**-bridged frameworks **6**.[33−35] The transformation of nonrigid **6** into the desired target **TzAF** was realized through the oxidation of the dihydro-**Tz** units into aromatic **Tz** rings in the frameworks.[33]

2.2. Characterization. The as-synthesized **TzAF** was characterized by suspended-state ^{1}H nuclear magnetic resonance (NMR) and solid-state ^{13}C cross-polarization magic angle spinning (^{13}C CP-MAS) NMR spectroscopies, Fourier transform infrared (FTIR) spectroscopy, ultraviolet−

Scheme 1. Synthesis of TzAF
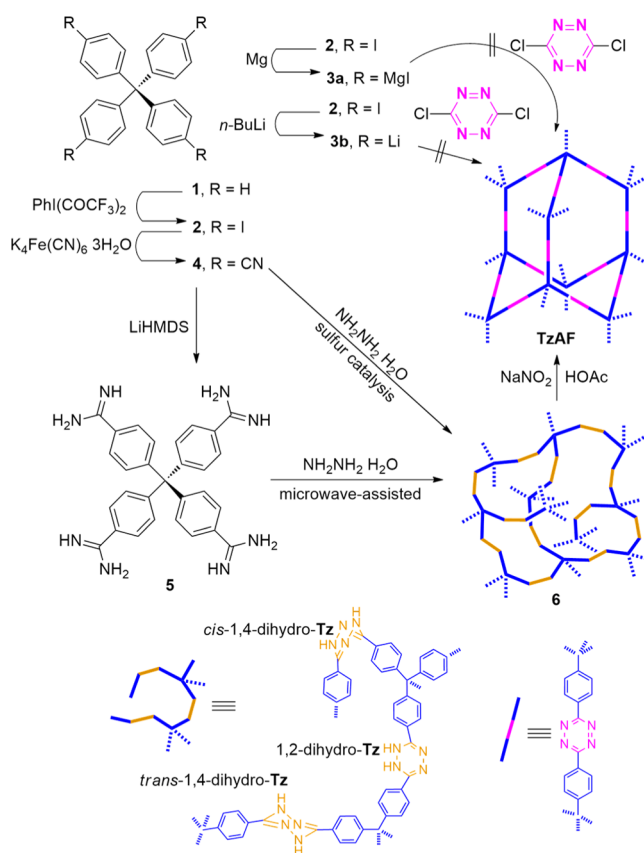
visible (UV−vis) spectroscopy, solid-state UV−vis−near-IR (UV−vis−NIR) spectroscopy, X-ray photoelectron spectroscopy (XPS), thermogravimetric analysis (TGA), powder X-ray diffraction (PXRD) analysis, field-emission scanning electron microscopy (FE-SEM), and field-emission transmission electron microscopy (FE-TEM). The aromatic protons were obvious in the suspended-state ^{1}H NMR spectrum of **TzAF** dispersed in DMSO-d_6 (Figure 1a), while no amidine NH proton signals in the range of 9−10 ppm were observed, indicating the complete conversion of **6** to **TzAF**.[36] The signals at around 65 ppm, 127−155 ppm, and 160−165 ppm in the ^{13}C CP-MAS NMR spectrum (Figure 1b) could be assigned to the carbons of tetraphenylmethanes, the benzene, and the **Tz** units, respectively. The peak at 42.7 ppm (7.5 kHz) should be attributed to the spinning sideband of the C−H carbons of benzene, which have a large chemical-shift anisotropy ($\Delta\delta$ = 127.7 ppm) (22.5 kHz); thus, the chemical shifts of the benzene C−H carbons and the sideband differed by ~15 kHz, which is the frequency of MAS. Other spinning sidebands and the artifacts of magic-angle spinning (MAS)[37,38] are shown in Figure S6 (Supporting Information).

In the UV−vis spectra of amidine **5** and **TzAF** dispersed in a water and ethanol solution (1:1, v/v) (Figure 1c), the broad absorption peaks in the range of 250−270 nm could be attributed to the $\pi-\pi*$ electron transition of the benzene rings.[39] As the benzene units in **TzAF** were covalently connected to the electron-deficient **Tz** units, their $\pi-\pi*$ electron transition absorption peak blue-shifted by 7 nm with respect to that of **5** (**TzAF**, 257.5 nm; **5**, 264.5 nm) (Figure 1c). **TzAF** also showed weak absorption in the range of 300−500 nm, which could be attributed to the $n-\pi*$ and $\pi-\pi*$
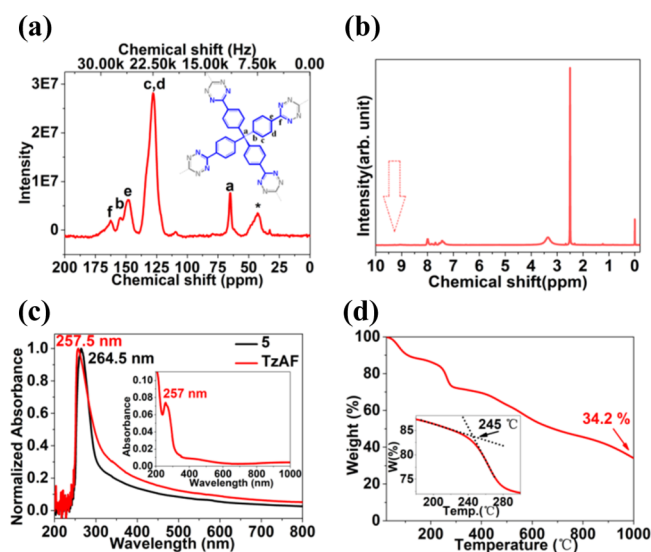
Figure 1. (a) Suspended-state ^1H NMR spectrum of **TzAF** dispersed in DMSO-d_6 (400 MHz, 298 K); (b) solid-state ^{13}C CP-MAS NMR spectrum of **TzAF**; (c) normalized UV−vis spectra of **5** (black) and **TzAF** (red) in a mixed solvent of water and ethanol (1:1, v/v) (insert: UV−vis−NIR spectrum of **TzAF** as a solid-state thin film); (d) TGA of **TzAF** under a N_2 atmosphere (insert: detailed view in the range of 180−300 °C).

electron transitions of the **Tz** units.[40] In the UV−vis−NIR spectrum of the solid **TzAF** thin film (Figure 1c, the insert), an absorption peak at ~257 nm ($\pi−\pi*$ transition of the benzene rings) and an absorption band ranging from 300 to 600 nm ($n−\pi*$ and $\pi−\pi*$ transitions of tetrazine units) were observed. The similarity between the UV−vis spectra of **TzAF** dispersed in the solution and **TzAF** film implied that **TzAF** is in homologous chemical environments in both the solution and solid state. TGA under a nitrogen atmosphere indicated that **TzAF** started to decompose at 245 °C (extrapolation, the insert of Figure 1d) probably due to the decomposition of the **Tz** units,[41,42] and ~35% weight remained at 1000 °C.

The X-ray photoelectron spectrum of **TzAF** (Figure 2) showed three peaks at 532, 400, and 285 eV, corresponding to O 1s, N 1s, and C 1s signals, respectively (Figure 2a). The O 1s peak mainly arose from molecular oxygen or water molecules absorbed on the surface or in the pores of the frameworks, which is typical for most carbon-based materials.[30,31,43] The N 1s peak with a binding energy of 400.1 eV was from the −C═N− of **Tz** rings (Figure 2b).[44] Since the charge distribution on carbon atoms in the **Tz** rings was influenced by the electron-deficient **Tz** N atoms, the C 1s peak of TzAF was deconvoluted into Gaussian−Lorentzian shapes (Figure 2c), among which the peak at 284.7 eV was assigned to quaternary carbons and phenyl carbons, the one at 285.5 eV to the carbons in the **Tz** units,[43−46] and the weak broad peak at 291.6 eV to the characteristic shake-up satellites of the aromatic carbons ($\pi−\pi*$ transition).[43,47−49]

In the FTIR spectrum of **TzAF** (Figure 3), the disappearance of the amidine −C═NH peak at 1676 cm^{-1} indicated no residual amidine left in the sample.[36,50,51] The IR bands at 1560, 1412, and 1072 cm^{-1} could arise from the C−N stretching vibrations of the **Tz** units,[52−55] and the peaks at 1609, 1493, and 1448 cm^{-1} corresponded to the C═C breathing vibrations of the benzene rings. Due to the effect of electron deficiency of the **Tz** units, the characteristic peak for
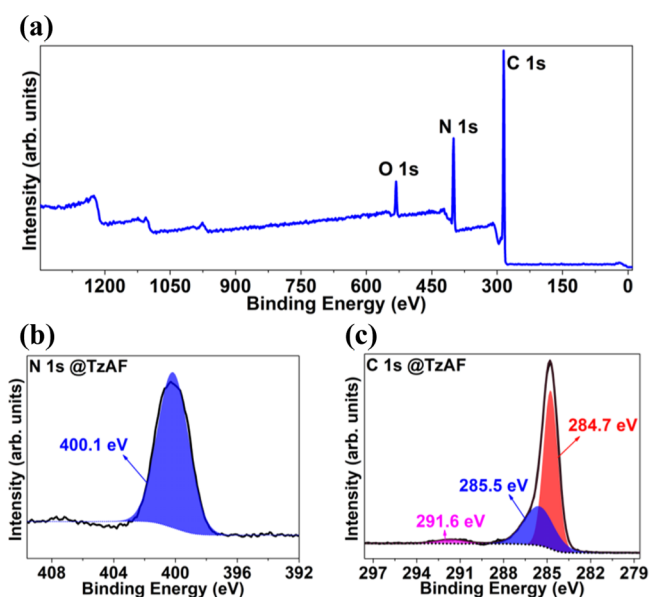

Figure 2. X-ray photoelectron spectrum of **TzAF**: (a) survey spectrum; (b) N 1s scan; (c) C 1s scan.
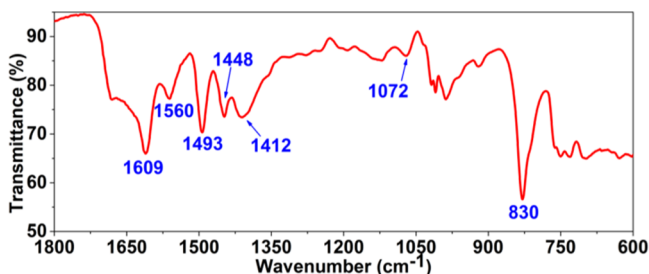

Figure 3. FTIR spectrum of **TzAF** in the range of 1800−600 cm^{-1}.

the benzene rings red-shifted from 1500 cm^{-1} to 1493 cm^{-1}, with its intensity reduced to a level lower than the peak at 1609 cm^{-1}.[56] Additionally, the absorption band at 830 cm^{-1} was attributed the characteristic C−H out-of-plane bending vibrations of the benzene units.

From the nitrogen adsorption−desorption measurement at 77 K, a type IV adsorption isotherm, typical for mesoporous materials, was obtained (Figure 4c).[57] The Brunauer−Emmett−Teller (BET) surface area of **TzAF** was calculated to be 16 $m^2\ g^{-1}$, and the pore size distribution calculated by the Barrett−Joyner−Halenda method showed that **TzAF** is a mesoporous material with the pore diameters ranging between 1.8 and 2.5 nm. The PXRD measurement (Figure 4b) of **TzAF** showed no apparent sharp peaks in 1−10° (2 theta), declaring its non-long-range ordering nature. The BET surface area of **TzAF** was obviously smaller than what we expected for such PAFs.[58,59] One possible reason could be structural interpenetration, which is hard to avoid in the formation of PAFs. In addition, we believe that incompletion of the formation of the ideal diamond-shaped lattice of the frameworks could be another reason. The nonaromatic dihydro-**Tz** is a nonplanar twisted ring, as illustrated by a model compound 3,6-dimethyl-1,4-dihydro-1,2,4,5-tetrazine (Figure S8, Supporting Information),[60] and twisted nonaromatic dihydro-**Tz** should cause structural twists in the intermediate frameworks **6**. Therefore, frameworks **6** could be semiporous, which could hinder $NaNO_2$ from diffusing freely into the mesopores of **6**, resulting
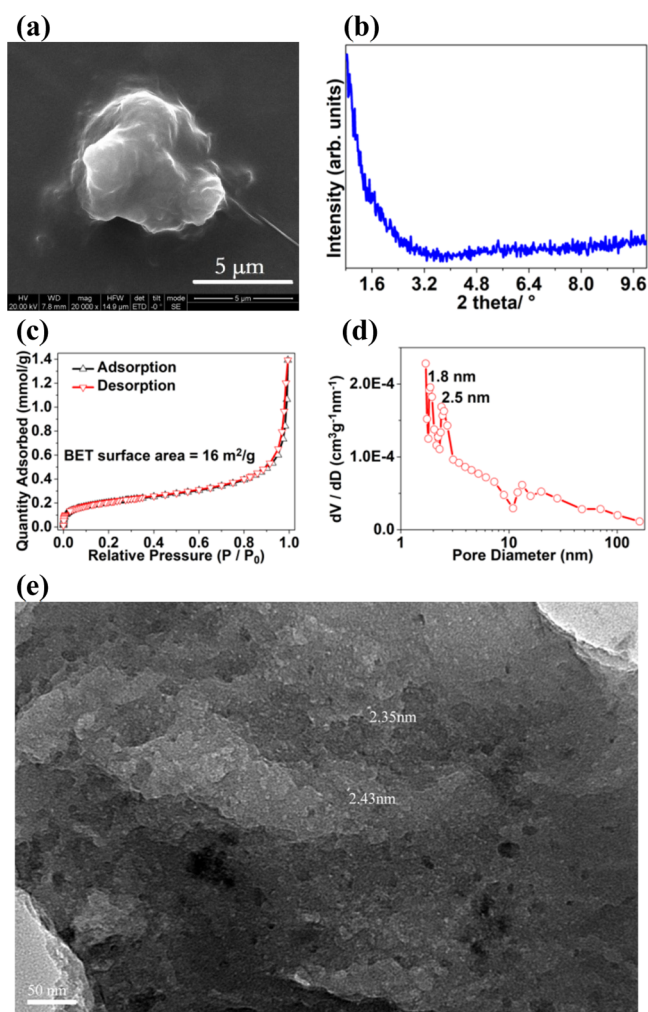
Figure 4. (a) FE-SEM image of **TzAF** (5 μm scale); (b) PXRD pattern of **TzAF** (2 theta = 0.8−10°); (c) nitrogen sorption isotherm of **TzAF** at 77 K; (d) pore size distribution of **TzAF**; (e) FE-TEM image of **TzAF** (50 nm scale).

in the incompletion of the oxidation of dihydro-**Tz** by $NaNO_2$. As a result, the aromatic frameworks **TzAF** could also be semiporous with mesopores (pore size ∼2 nm), which is consistent with a low BET surface area value.

The morphological details of **TzAF** were studied by FE-TEM and FE-SEM. The FE-SEM images of **TzAF** revealed particulates in the microscale (Figure 4a and Supporting Information), while the FE-TEM images with a relatively small thickness contrast indicated that the pore sizes were about 2 nm, which was consistent with the result of nitrogen adsorption−desorption measurement (Figure 4e and Supporting Information).

2.3. Fluorescence Properties. In order to get a better understanding of the fluorescence property of **TzAF**, 3,6-di-*p*-tolyl-1,2,4,5-tetrazine (**DTTz**) was prepared as a model structure of the **TzAF** skeleton unit. The quantum chemical calculations of **DTTz** revealed an absence of imaginary frequencies, which meant a true energy minimum, consistent with its crystal structure (CCDC 202204).[61] Based on the optimized geometry of **DTTz**, the optical transition energies and oscillator strengths were obtained using time-dependent density functional theory (TD-DFT) calculations with the same basic set. The results of the TD-DFT calculations (Figure

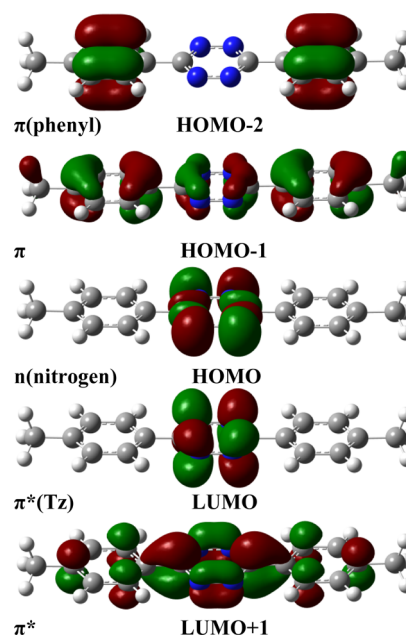5 and Table S1, Supporting Information) agreed well with the experimental UV−vis spectrum (Figure 6b).

Figure 5. Plots of the calculated molecular orbitals of **DTTz** (blue, O; gray, C; white, H).

The leading configuration of the first excited state is an n−π^* transition (S_0−S_1), that is, from the nonbonding orbitals of the nitrogen atoms highest occupied molecular orbital (HOMO) in **DTTz** to the antibonding π^* orbitals of the **Tz** ring (LUMO). The oscillator strength is low as a result of this forbidden transition, which is also in agreement with the experimental result where the corresponding absorption band is weak (centered at 543.5 nm, ε = 354 L mol^{-1} cm^{-1}). The shoulder-type peak range of 350−420 nm in the experimental spectrum is a weak π−π^* transition (Figure 6b) which might involve π-orbitals delocalized over the **DTTz** molecule (HOMO − 1 → LUMO). Meanwhile, an intermediate transition which involves n−π^* transition (HOMO → LUMO + 1) is calculated to be with a zero oscillator strength. The absorption band at around 300 nm arises from the combination of two π−π^* transitions: one from the orbitals of the **Tz** ring and the other from the orbitals of the benzene-ring.

Upon excitation at the first absorption (500−600 nm) of **DTTz**, weak fluorescence was observed in the region of 575−620 nm (Figure 6a). In addition, a higher absorption energy leads to a higher excited (S_n) state, which could be transformed to the S_1 state through vibrational relaxation and internal conversion, accompanied by emitting S_1 → S_0 or S_n → S_0 fluorescence.[38] As a consequence, the excitation of **DTTz** by a 330−400 nm light resulted in fluorescent emission at 560−630 nm. The inconspicuously weak fluorescence peak at around 580 nm might be due to the intermolecular orbital overlap between the electron-deficient **Tz** ring and the two electron-rich benzene rings in **DTTz**. Nevertheless, the orbital overlap between **Tz** units and benzene units in the frameworks **TzAF** was prohibited due to the blockage of quaternary carbons. Consequently, solvent-dispersed **TzAF** emitted fluorescence at 400−650 nm at a higher intensity with two broad excitation wavelength ranges of 270−310 nm and 350−600 nm (Figure 6c). In addition, the PL spectra of the solid-state **TzAF** excited
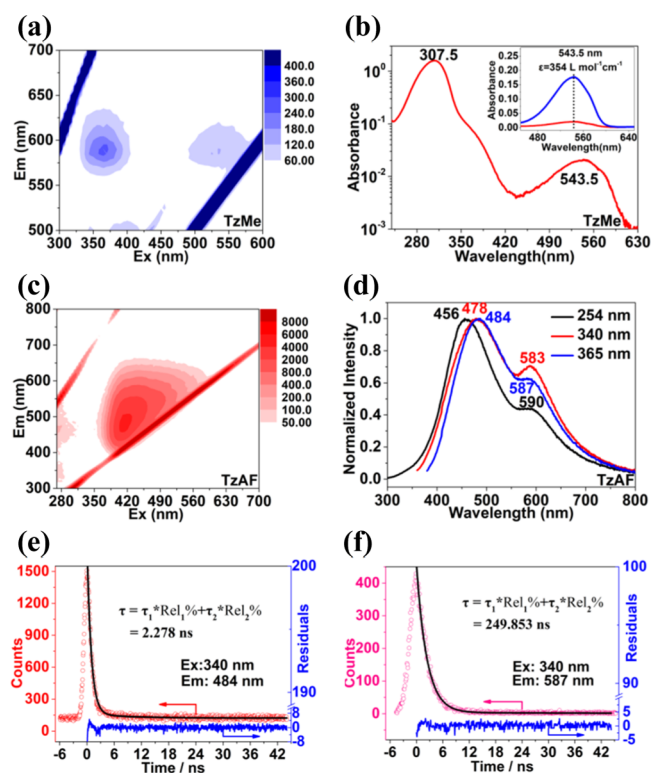
Figure 6. (a) 3D-fluorescence spectrum of **DTTz** (5×10^{-4} M in MeCN) in the range of 500−700 nm (excited by 300−600 nm). (b) UV−vis spectrum of **DTTz** in MeCN (red, 5×10^{-5} M; blue, 5×10^{-4} M). (c) 3D-fluorescence spectrum of **TzAF** (in a mixed solvent of Et$_3$N/MeOH, 1:10, v/v) in the range of 300−800 nm (excited by 270−800 nm). (d) PL spectra of the solid-state **TzAF** excited at 254 nm (black), 340 nm (red), and 365 nm (blue). (e) Fluorescence time profile of **TzAF** ($\lambda_{exc.} = 340$ nm and $\lambda_{dec.} = 484$ nm): the experimental data (red), fitting curve (black), and residuals (blue). (f) Fluorescence time profile of **TzAF** ($\lambda_{exc.} = 340$ nm and $\lambda_{dec.} = 587$ nm): the experimental data (purple), fitting curve (black), and residuals (blue).

at 254, 340, and 365 nm showed two broad emission peaks: one centered at 456, 478, and 484 nm and the other centered at 590, 583, and 587 nm, respectively (Figure 6d). The fitted lifetimes of **TzAF**'s fluorescence at 484 and 587 nm (excited by 340 nm) were 2.278 ns ($\tau_1 = 0.9157$ ns, 81.13%; $\tau_2 = 8.1241$ ns, 18.87%) and 249.853 ns ($\tau_1 = 2.3733$ ns, 23.18%; $\tau_2 = 324.5291$ ns, 76.82%), respectively, indicating that the emission at 587 nm needs more time to be vibrationally relaxed and internally converted to its S_1 state.

2.4. Fluorescence Switching.
The π-aromatic **Tz** ring can be reduced to a radical anion which has much weaker fluorescence emission than its neutral state, as exemplified by chloromethoxytetrazine.[16,17,19,20] Thus, in **TzAF**, the electron-deficient **Tz** units conjugated to the benzene units should be able to be readily reduced to **Tz** radical anions by light-generated electrons, resulting in a significant decrease in the fluorescence intensity. The fluorescence intensity could be able to be regained once the **Tz** radical releases an electron to resume the neutral state. Therefore, we envisioned that this neutral ↔ radical state interconversion should make **TzAF** a good photochromic fluorophore with distinct on−off fluorescence emission.

Based on the above assumptions, we set out to explore the fluorescence photoswitchability of the **TzAF** thin films coated on silica gel plates. As shown in Figure 6d, **TzAF** emitted

fluorescence under UV light irradiation at 365, 340, or 254 nm. To our delight, it was found that the **TzAF** thin film emitted bright fluorescence under a 254 nm UV light irradiation (Figure 7a), but its emission could be turned off by the
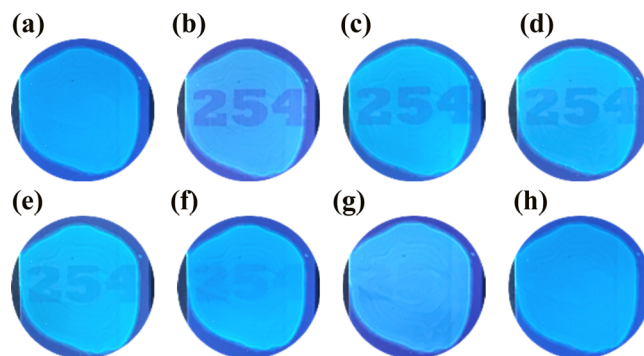

Figure 7. Images of the **TzAF** thin film coated on a silica gel plate. The nonfluorescent "254" was written using a laser beam (405 nm, 50 mW, 80 millisecond per point, and 5 dots per millimeter) and then exposed to 254 nm UV light (1.81 mW/cm^2). The photographs were taken under a 254 nm UV light before writing (a) at various time points: time = 0 (b), 10 s (c), 30 s (d), 1 min (e), 2 min (f), 5 min (g), and 10 min (h).

irradiation of a 405 nm laser light, as was exemplified by "writing" the number "254" on a 254 nm UV-excited **TzAF** thin film using 405 nm laser beam (Figure 7b and S13, Supporting Information). The mark"254" on the **TzAF** thin film started to fade when exposed to 254 nm UV light and disappeared thoroughly within 10 min (Figure 7c−h).

UV light at 365 nm functioned similarly in restoring the bright fluorescence emission of the **TzAF** thin film (see Figure S16 in the Supporting Information). In the repeatability test of the **TzAF** thin film's fluorescence photoswitching capability, the "writing" and "erasing" with 405 and 254 nm (or 365 nm) light irradiation were conducted for consecutive cycles without resulting in any identifiable difference in the behaviors of the thin film (Figures 8 and S17−S18, Supporting Information). It is worth noting that the mark written on the **TzAF** thin film by 405 nm irradiation did not last for 24 h under natural room light illumination (300−1000 nm) but lasted for no less than 70 days in the dark (Figure S15, Supporting Information).

We postulated that the on/off fluorescence emission of **TzAF** is attributed to the interconversion between **TzAF'** neutral ↔ radical states: **Tz** units in the neutral **TzAF** were reduced to radicals by 405 nm light-generated electrons, and the radicals lost electrons to get back to the neutral form under 254 nm UV light. In order to provide evidence to support this postulation, electron paramagnetic resonance (EPR) measurement was conducted. As shown in Figure 9a,b, a clear EPR signal was observed for **TzAF** irradiated by 405 nm light (red curve), and such a signal could not be seen in the dark or before light irradiation (black curve). The g-factor spectrum (Figure 9b) of **TzAF** after 405 nm light irradiation was derived from Figure 9a and indicated that the experimental g-factor was 2.00429, typical for nitrogen-centered radicals.[62] Therefore, the shutting off of the fluorescence emission of **TzAF** can be attributed to the transformation of fluorescent neutral **TzAF** to its nonfluorescent radical state. The photogenerated electron in the **TzAF** radical is considered in its singly occupied molecular orbital excited by a higher energy 365 or 254 nm
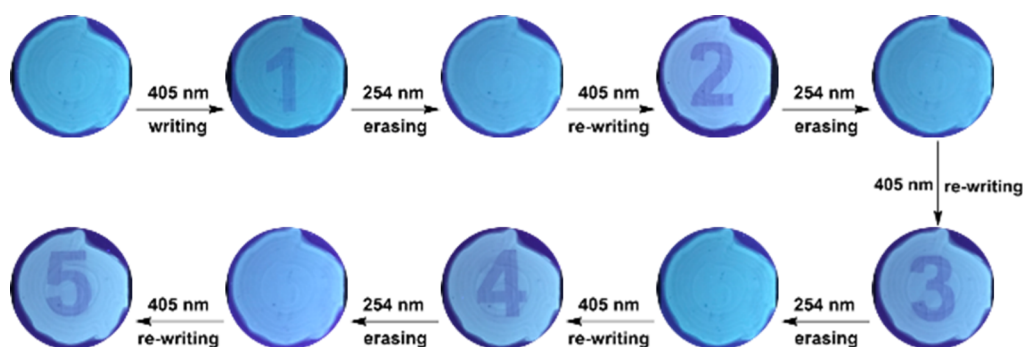
Figure 8. Repeatability of **TzAF** thin film's fluorescence photoswitching. The numbers 1−5 were written using a laser beam (405 nm, 50 mW, 80 millisecond per point and 5 dots per millimeter), and the numbers 1−4 were erased by exposure under 254 nm UV light (1.81 mW/cm^2) for 10 min.
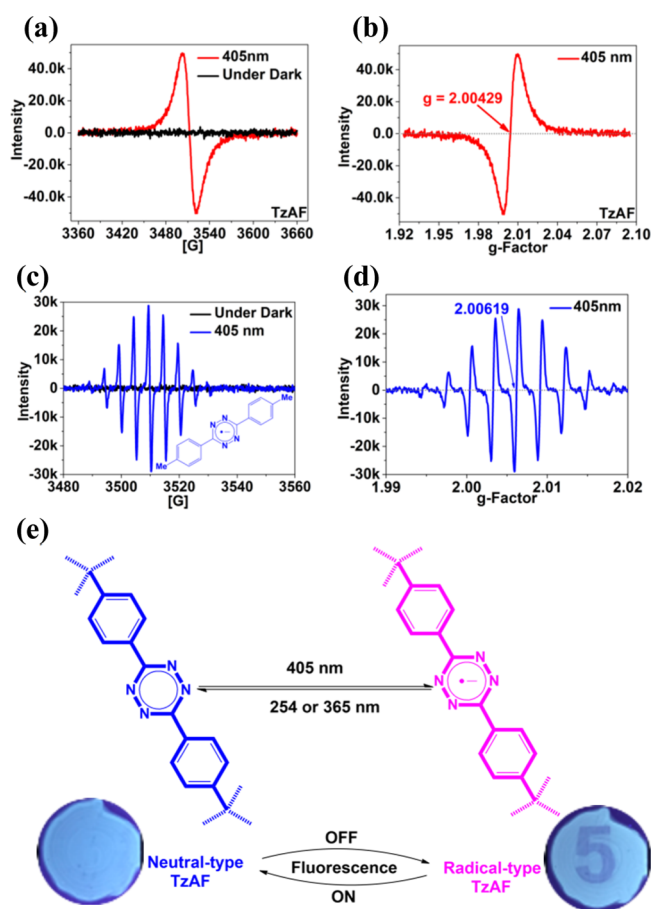

Figure 9. (a) EPR/ESR spectra of **TzAF** (black: in the dark; red: after 405 nm irradiation). Microwave (MW) frequency 9.852 GHz; MW power, 19.10 mW; modulation amplitude, 1.00 G; time constant, 10.24 ms; and sweep time: 30.72 s; (b) g-factor spectrum of **TzAF** in the EPR/ESR test. (c) EPR/ESR spectra of solid-state **DTTz** (black: under the dark; blue: after 405 nm irradiation). (MW frequency 9.855 GHz; MW power, 19.61 mW; modulation amplitude, 1.00 G; time constant, 10.24 ns; and sweep time, 60.42 s; (d) g-factor spectrum of solid-state **DTTz** in the EPR/ESR test. (e) The "on/off" fluorescence emission of **TzAF** and the reversible transformation between its neutral and radical states.

light irradiation, followed by de-excitation to its ground state accompanied with the reproduction of fluorescence.

With the mechanism of **TzAF**'s "on/off" fluorescence emission elucidated, we wanted to find out whether a single

unit of **TzAF** possesses such fluorescent photoswitchability. Thus, we conducted EPR analysis of **DTTz**, the model compound of a single unit of **TzAF**, in its solid-state (Figure 9c,d) and in CH$_3$CN solution (Figure S21, Supporting Information). The intensity ratio of characteristic signals obtained was 1.34:4.41:9.88:16.07:18.63:16.38:10.34:4.04:1.59 (Figure 9c), consistent with the theoretical value calculated for **Tz**-type radicals (1:4:10:16:19:16:10:4:1).[63] However, there was a significant difference between the frameworks **TzAF** and the monomer **DTTz**: neither the **DTTz** thin film nor **DTTz** solution (in CH$_3$CN) showed such a switchable "on/off" emission property (Figure S20, Supporting Information). In **TzAF**, the **Tz** radical anion was stabilized by delocalization of the electron over the **Tz** ring and the two conjugated phenyl rings. In addition, Ph-**Tz**-Ph type-radical anion units in **TzAF** were isolated by the quaternary carbons, which further improved the stability of the radical anions in a similar way to the encapsulation strategy reported by Flood's group.[64] A naked **DTTz** radical anion does not have such a protection; thus, it lacks such fluorescence switchability.

3. CONCLUSIONS

s-Tetrazine (**Tz**), arguably the smallest fluorophore was incorporated in the skeleton of PAFs for the first time, resulting in photochromic aromatic frameworks **TzAF**. A thin film of the as-synthesized **TzAF** was found to possess a consecutive "writing/erasing" property through the irradiation of 405 and 254 nm (or 365 nm) light, respectively, which could be mechanistically attributed to the "on/off" fluorescence photoswitchability resulting from reversible transformation between fluorescent-neutral and nonfluorescent radical states. The rigid skeleton of **TzAF** provided a protective environment for stabilization of the photogenerated **Tz** radicals, while aggregation-caused quenching (ACQ) resulted in the loss of fluorescence photoswitchability for **DTTz** in the solid state. The unique fluorescent photochromic **TzAF** should have potential in various optoelectronic applications, including optical memories, bioimaging, and photoswitches with high sensitivity.

4. EXPERIMENTAL SECTION

4.1. General. Unless otherwise noted, the reagents and solvents were purchased from commercial sources and used as received. The ^{1}H and ^{13}C NMR spectra were recorded on a Bruker AVANCE III HD 500 NMR spectrometer or a Bruker AVANCE NEO 400 spectrometer. ^{13}C cross-polarization MAS

NMR (^{13}C CP/MAS NMR) spectra were recorded on a Bruker AVANCE Neo 700 MHz spectrometer. Electrospray ionization mass spectrometry analysis was conducted on a Thermo Scientific Q Exactive Focus mass spectrometer with an UltiMate 3000 RSLC high-performance liquid chromatography system. TGA was carried out on a Mettler Toledo TGA/DSC 3 + thermogravimetric analyzer, and the samples were heated to 1000 °C at a heating rate of 10 °C/min under a N_2 atmosphere. The PXRD measurements were carried out on a Bruker AXS D8 ADVANCE X-ray diffractometer with Cu Kα as the radiation source (λ = 1.5418 Å) and operated at 40 kV and 40 mA. The surface area, nitrogen adsorption isotherms (77 K), and pore size distributions were measured using an ASAP 2020 HD accelerated surface area and porosimetry system, and the sample was degassed at 90 °C for 6 h prior to analysis. The Fourier transform IR (FTIR) spectra were obtained on a Thermo Scientific Nicolet iS5 FTIR spectrometer using the attenuated total reflection technique, and the sample was dried in an IR oven equipped with two 275 W lamps prior to the test. The UV−vis spectra were recorded on a UV-8000S Double Beam UV/vis spectrophotometer (Shanghai Precision Instruments) and the UV−vis−NIR spectra on an Agilent Cary UV−vis−NIR spectrophotometer. EPR/electron spin resonance (ESR) spectra were obtained on a Bruker EPR A300 spectrometer. The morphological details were studied using FE-SEM (on a FEI Inspect F50) and FE-TEM (on a JEM-2100F field emission electron microscope). The XPS analysis was conducted on a Thermo Fisher ESCALAB 250 Xi X-ray photoelectron spectrometer. Structural simulation was performed using BIOVIA Materials Studio Forcite (geometry optimization: energy, 2×10^{-5} kcal/mol; force, 0.001 kcal/(mol Å); stress, 0.001 GPa; displacement, 1.0×10^{-5} Å). Control software in fluorescence photoswitching was obtained from VigoTec, and calculations were performed at the B3LYP/6-311+G(d) level using Gaussian 09 Revision E.01.

4.2. Tetra(4-iodophenyl)-methane (2). A suspension of iodine (9.23 g, 36.0 mmol), tetraphenylmethane (3.92 g, 12.0 mmol), and bis(trifluoroacetoxy)iodobenzene (13.2 g, 30.0 mmol) in CCl_4 (180 mL) was refluxed under N_2 for 10 h, cooled to room temperature, and filtered to collect the solid which was washed with petroleum ether and dried at 100 °C under reduced pressure for 1 h to afford **2** (6.4 g, 65%) as a light-pink powder. ^{1}H NMR (500 MHz, DMSO-d_6): δ 7.69 (8H), 6.91(8H).

4.3. Tetra(4-cyanophenyl)-methane (4). A mixture of tetra(4-iodophenyl)-methane (**2**) (1.32 g, 1.6 mmol), K_4Fe-(CN)$_6$·3H$_2$O (1.40 g, 3.3 mmol), K_2CO_3 (0.68 g, 4.92 mmol), and Pd(OAc)$_2$ (35.9 mg, 0.16 mmol) in dimethylformamide (25 mL) was purged with N_2, heated at 150 °C for 18 h, cooled to room temperature, poured into DCM (50 mL), and filtered to remove the solids. The filtrate was concentrated to result in a residue which was subjected to chromatography (petroleum ether/DCM = 1:1) to afford **4** as a white powder. ^{1}H NMR (500 MHz, DMSO-d_6): δ 7.83 (d, 8.4 Hz, 8H) 7.42 (d, 8.3 Hz, 8H); ^{13}C NMR (125 MHz, DMSO-d_6): δ 149.6, 132.9, 131.5, 118.8, 110.3, 65.9.

4.4. 4,4′,4″,4‴-Methanetetrayltetrabenzimidamide Tetrahydrochloride (5). To a solution of tetra(4-cyanophenyl)-methane (**4**) (353 mg, 0.84 mmol) in dry THF (20 mL) under N_2 was added a solution of LiHMDS in THF (1.0 M, 7.5 mL, 7.5 mmol) at—84 °C (EtOAc-liquid nitrogen bath). The resulting mixture was warmed to room temperature

and stirred for 18 h to form a yellowish-orange solution which was then cooled to 0 °C. After an ethanolic HCl solution (12 mL, 32 mL, freshly prepared by adding acetyl chloride to ethanol) was added, the precipitate collected by filtration was suspended in 10 mL of ethanol, sonicated for 1 h, filtered to remove the solvent, and dried under reduced pressure to afford **5** as a cream-colored solid (525 mg, 98%). ^{1}H NMR (500 MHz, D$_2$O): δ 7.77 (d, 8.5 Hz, 8H) 7.62 (d, 8.6 Hz, 8H); ^{13}C NMR (125 MHz, D$_2$O): δ 165.9, 150.7, 131.3, 127.8, 126.2, 65.4.

4.5. TzAF. To a suspension of 4,4′,4″,4‴-methanetetrayltetrabenzimidamide tetrahydrochloride (**5**) (64 mg, 0.1 mmol) in water (2.0 mL) was added hydrazine hydrate (46 μL, 85%, 0.8 mmol, 8 equiv), resulting in a mixture which was heated at 40 °C using MW for 1 h. The faint yellow precipitate was collected, suspended in an aqueous NaNO$_2$ solution (0.5 M, 2.0 mL), sonicated for 5 min, and cooled down to 0 °C in an ice-water bath. After glacial acetic acid (3×35 μL) was added portionwise under vigorous stirring, the pale-yellow precipitate disappeared, resulting in a pink solution which gradually became cloudy pink. After water (16 mL) was added, the reaction mixture was transferred into a regenerated cellulose dialysis bag for water dialysis three times and dried under reduced pressure at 120 °C to afford **TzAF** as a pink powder (33 mg).

■ ASSOCIATED CONTENT

Ⓢ Supporting Information

The Supporting Information is available free of charge at https://pubs.acs.org/doi/10.1021/acsomega.2c00278.

> ^{1}H NMR spectra, ^{13}C NMR spectra, and additional results (PDF)
>
> Laser writing step (MP4)

■ AUTHOR INFORMATION

Corresponding Authors

Weibo Hu − *Shanghai Advanced Research Institute, Chinese Academy of Sciences, Shanghai 201210, China;* ⓞ orcid.org/0000-0003-0301-0813; Email: huwb@sari.ac.cn

Hui Yang − *Shanghai Advanced Research Institute, Chinese Academy of Sciences, Shanghai 201210, China; School of Physical Science and Technology, ShanghaiTech University, Shanghai 201210, China;* ⓞ orcid.org/0000-0001-5013-0469; Email: yangh@sari.ac.cn

Ke Wen − *Shanghai Advanced Research Institute, Chinese Academy of Sciences, Shanghai 201210, China; School of Physical Science and Technology, ShanghaiTech University, Shanghai 201210, China;* ⓞ orcid.org/0000-0002-9717-4351; Email: wenk@sari.ac.cn

Authors

Tao Chen − *Shanghai Advanced Research Institute, Chinese Academy of Sciences, Shanghai 201210, China; University of Chinese Academy of Sciences, Beijing 100049, China;* ⓞ orcid.org/0000-0001-6110-9112

Guangjun Xiao − *Shanghai Advanced Research Institute, Chinese Academy of Sciences, Shanghai 201210, China; School of Physical Science and Technology, ShanghaiTech University, Shanghai 201210, China*

Zhuo Wang − *Shanghai Advanced Research Institute, Chinese Academy of Sciences, Shanghai 201210, China; School of Physical Science and Technology, ShanghaiTech University,*

Shanghai 201210, China; ● orcid.org/0000-0003-0432-7011

Jian Zou − Shanghai Advanced Research Institute, Chinese Academy of Sciences, Shanghai 201210, China; University of Chinese Academy of Sciences, Beijing 100049, China

Jian Wang − School of Life Science and Technology, ShanghaiTech University, Shanghai 201210, China

Yahu A. Liu − Medicinal Chemistry, ChemBridge Research Laboratories, San Diego, California 92127, United States; ● orcid.org/0000-0002-9434-6453

Notes
The authors declare no competing financial interest.

■ REFERENCES

(1) Theato, P.; Sumerlin, B. S.; O'Reilly, R. K.; Epps, T. H. Stimuli Responsive Materials. Chem. Soc. Rev. 2013, 42, 7055−7056.

(2) Wei, M.; Gao, Y.; Li, X.; Serpe, M. J. Stimuli-Responsive Polymers and Their Applications. Polym. Chem. 2017, 8, 127−143.

(3) Castiglioni, F.; Danowski, W.; Perego, J.; Leung, F. K.-C.; Sozzani, P.; Bracco, S.; Wezenberg, S. J.; Comotti, A.; Feringa, B. L. Modulation of Porosity in a Solid Material Enabled by Bulk Photoisomerization of an Overcrowded Alkene. Nat. Chem. 2020, 12, 595−602.

(4) Brighenti, R.; Li, Y.; Vernerey, F. J. Smart Polymers for Advanced Applications: A Mechanical Perspective Review. Front. Mater. Sci. 2020, 7, 196.

(5) Cook, A. B.; Decuzzi, P. Harnessing Endogenous Stimuli for Responsive Materials in Theranostics. ACS Nano 2021, 15, 2068−2098.

(6) Yang, P.; Zhu, F.; Zhang, Z.; Cheng, Y.; Wang, Z.; Li, Y. Stimuli-Responsive Polydopamine-Based Smart Materials. Chem. Soc. Rev. 2021, 50, 8319−8343.

(7) Fukaminato, T.; Ishida, S.; Métivier, R. Photochromic Fluorophores at The Molecular and Nanoparticle Levels: Fundamentals and Applications of Diarylethenes. NPG Asia Mater. 2018, 10, 859−881.

(8) Baroncini, M.; d'Agostino, S.; Bergamini, G.; Ceroni, P.; Comotti, A.; Sozzani, P.; Bassanetti, I.; Grepioni, F.; Hernandez, T. M.; Silvi, S.; Venturi, M.; Credi, A. Photoinduced Reversible Switching of Porosity in Molecular Crystals Based on Star-Shaped Azobenzene Tetramers. Nat. Chem. 2015, 7, 634−640.

(9) Raymo, F. M. Photoactivatable Synthetic Fluorophores. Phys. Chem. Chem. Phys. 2013, 15, 14840−14850.

(10) Zhang, J.; Zou, Q.; Tian, H. Photochromic Materials: More Than Meets The Eye. Adv. Mater. 2013, 25, 378−399.

(11) Mutoh, K.; Miyashita, N.; Arai, K.; Abe, J. Turn-On Mode Fluorescence Switch by Using Negative Photochromic Imidazole Dimer. J. Am. Chem. Soc. 2019, 141, 5650−5654.

(12) Heilemann, M.; Dedecker, P.; Hofkens, J.; Sauer, M. Photoswitches: Key Molecules for Subdiffraction-resolution Fluorescence Imaging and Molecular Quantification. Laser Photon. Rev. 2009, 3, 180−202.

(13) Benson, C. R.; Kacenauskaite, L.; VanDenburgh, K. L.; Zhao, W.; Qiao, B.; Sadhukhan, T.; Pink, M.; Chen, J.; Borgi, S.; Chen, C.-H.; Davis, B. J.; Simon, Y. C.; Raghavachari, K.; Laursen, B. W.; Flood, A. H. Plug-and-Play Optical Materials from Fluorescent Dyes and Macrocycles. Chem 2020, 6, 1978−1997.

(14) Huang, Y.; Xing, J.; Gong, Q.; Chen, L.-C.; Liu, G.; Yao, C.; Wang, Z.; Zhang, H.-L.; Chen, Z.; Zhang, Q. Reducing Aggregation Caused Quenching Effect through Co-assembly of PAH Chromophores and Molecular Barriers. Nat. Commun. 2019, 10, 169.

(15) Haug, W. K.; Moscarello, E. M.; Wolfson, E. R.; McGrier, P. L. The Luminescent and Photophysical Properties of Covalent Organic Frameworks. Chem. Soc. Rev. 2020, 49, 839−864.

(16) Chen, D.; Liu, C.; Tang, J.; Luo, L.; Yu, G. Fluorescent Porous Organic Polymers. Polym. Chem. 2019, 10, 1168−1181.

(17) Kundu, P. K.; Olsen, G. L.; Kiss, V.; Klajn, R. Nanoporous Frameworks Exhibiting Multiple Stimuli Responsiveness. Nat. Commun. 2014, 5, 3588.

(18) Lyndon, R.; Konstas, K.; Evans, R. A.; Keddie, D. J.; Hill, M. R.; Ladewig, B. P. Tunable Photodynamic Switching of DArE@PAF-1 for Carbon Capture. Adv. Funct. Mater. 2015, 25, 4405−4411.

(19) Ma, T.; Zhao, X.; Matsuo, Y.; Song, J.; Zhao, R.; Faheem, M.; Chen, M.; Zhang, Y.; Tian, Y.; Zhu, G. Fluorescein- based Fluorescent Porous Aromatic Framework for Fe^{3+} Detection with High Sensitivity. J. Mater. Chem. C 2019, 7, 2327−2332.

(20) Clavier, G.; Audebert, P. s-Tetrazines as Building Blocks for New Functional Molecules and Molecular Materials. Chem. Rev. 2010, 110, 3299−3314.

(21) Kerth, J.; Löbbecke, S. Synthesis and Characterization of 3,3'-Azobis(6-Amino-1,2,4,5-Tetrazine) DAAT − A New Promising Nitrogen-Rich Compound. Propellants, Explos., Pyrotech. 2002, 27, 111−118.

(22) Miomandre, F.; Audebert, P. 1,2,4,5-Tetrazines: An Intriguing Heterocycles Family with Outstanding Characteristics in The Field of Luminescence and Electrochemistry. J. Photochem. Photobiol., C 2020, 44, 100372.

(23) Kim, Y.; Kim, E.; Clavier, G.; Audebert, P. New Tetrazine-based Fluoroelectrochromic Window; Modulation of The Fluorescence through Applied Potential. Chem. Commun. 2006, 34, 3612−3614.

(24) Kim, Y.; Do, J.; Kim, E.; Clavier, G.; Galmiche, L.; Audebert, P. Tetrazine-based Electrofluorochromic Windows: Modulation of The Fluorescence through Applied Potential. J. Electroanal. Chem. 2009, 632, 201−205.

(25) Li, Z.; Ding, J.; Song, N.; Du, X.; Zhou, J.; Lu, J.; Tao, Y. Alternating Copolymers of Dithienyl-s-Tetrazine and Cyclopentadithiophene for Organic Photovoltaic Applications. Chem. Mater. 2011, 23, 1977−1984.

(26) Xu, X.; Feng, K.; Bi, Z.; Ma, W.; Zhang, G.; Peng, Q. Single-Junction Polymer Solar Cells with 16.35% Efficiency Enabled by a Platinum(II) Complexation Strategy. Adv. Mater. 2019, 31, 1901872.

(27) Li, Z.; Ding, J.; Song, N.; Lu, J.; Tao, Y. Development of a New s-Tetrazine-Based Copolymer for Efficient Solar Cells. J. Am. Chem. Soc. 2010, 132, 13160−13161.

(28) Lu, Z.-Z.; Zhang, R.; Li, Y.-Z.; Guo, Z.-J.; Zheng, H.-G. Solvatochromic Behavior of a Nanotubular Metal-Organic Framework for Sensing Small Molecules. J. Am. Chem. Soc. 2011, 133, 4172−4174.

(29) Ghosh, S.; Nakada, A.; Springer, M. A.; Kawaguchi, T.; Suzuki, K.; Kaji, H.; Baburin, I.; Kuc, A.; Heine, T.; Suzuki, H.; Abe, R.; Seki, S. Identification of Prime Factors to Maximize the Photocatalytic Hydrogen Evolution of Covalent Organic Frameworks. J. Am. Chem. Soc. 2020, 142, 9752−9762.

(30) Chen, T.; Li, W. Q.; Chen, X. J.; Guo, Y. Z.; Hu, W. B.; Hu, W. J.; Liu, Y. A.; Yang, H.; Wen, K. A Triazine-Based Analogue of Graphyne: Scalable Synthesis and Applications in Photocatalytic Dye Degradation and Bacterial Inactivation. Chem. - Eur. J. 2020, 26, 2269−2275.

(31) Chen, T.; Li, W.-Q.; Hu, W.-B.; Hu, W.-J.; Liu, Y. A.; Yang, H.; Wen, K. Direct Synthesis of Covalent Triazine-Based Frameworks (CTFs) through Aromatic Nucleophilic Substitution Reactions. RSC Adv. 2019, 9, 18008−18012.

(32) Pan, Q.; Chen, T.; Ma, L.; Wang, G.; Hu, W.-B.; Zou, Z.; Wen, K.; Yang, H. Covalent Triazine-Based Polymers with Controllable Band Alignment Matched with BiVO4 To Boost Photogeneration of Holes for Water Splitting. *Chem. Mater.* **2019**, *31*, 8062−8068.

(33) Audebert, P.; Sadki, S.; Miomandre, F.; Clavier, G.; Claude Vernières, M.; Saoud, M.; Hapiot, P. Synthesis of New Substituted Tetrazines: Electrochemical and Spectroscopic Properties. *New J. Chem.* **2004**, *28*, 387−392.

(34) Polezhaev, A. V.; Maciulis, N. A.; Chen, C.-H.; Pink, M.; Lord, R. L.; Caulton, K. G. Tetrazine Assists Reduction of Water by Phosphines: Application in the Mitsunobu Reaction. *Chem. - Eur. J.* **2016**, *22*, 13985−13998.

(35) Rao, G.-W.; Hu, W.-X. Synthesis, Structure Analysis, and Antitumor Activity of 3,6-disubstituted-1,4-dihydro-1,2,4,5-tetrazine Derivatives. *Bioorg. Med. Chem. Lett.* **2006**, *16*, 3702−3705.

(36) Morshedi, M.; Thomas, M.; Tarzia, A.; Doonan, C. J.; White, N. G. Supramolecular Anion Recognition in Water: Synthesis of Hydrogen-bonded Supramolecular Frameworks. *Chem. Sci.* **2017**, *8*, 3019−3025.

(37) Thakur, K. A. M.; Kean, R. T.; Zupfer, J. M.; Buehler, N. U.; Doscotch, M. A.; Munson, E. J. Solid State ^{13}C CP-MAS NMR Studies of the Crystallinity and Morphology of Poly(l-lactide). *Macromolecules* **1996**, *29*, 8844−8851.

(38) Lee, Y. J.; Grey, C. P. Determining the Lithium Local Environments in the Lithium Manganates LiZn$_{0.5}$Mn$_{1.5}$O$_4$ and Li$_2$MnO$_3$ by Analysis of the ^{6}Li MAS NMR Spinning Sideband Manifolds. *J. Phys. Chem. B* **2002**, *106*, 3576−3582.

(39) Barker, P. L.; Gendler, P. L.; Rapoport, H. Acylation of Dibasic Compounds Containing Amino Amidine and Aminoguanidine Functions. *J. Org. Chem.* **1981**, *46*, 2455−2465.

(40) Topp, K.-D.; Grote, M. Synthesis and Characterization of a 1,2,4,5-tetrazine-modified Ion-exchange Resin. *React. Funct. Polym.* **1996**, *31*, 117−136.

(41) Löbbecke, S.; Pfeil, A.; Krause, H. H.; Sauer, J.; Holland, U. Thermoanalytical Screening of Nitrogen-Rich Substances. *Propellants, Explos., Pyrotech.* **1999**, *24*, 168−175.

(42) Xiong, Y.; Shu, Y.-J.; Wang, X.-F.; Zong, H.-H.; Zhou, Y.; Yin, M. Theoretical Study on Effect of Tetrazine Structures on Their Thermal Decomposition Mechanisms. *Chin. J. Explos. Propellants* **2008**, *31*, 1−5.

(43) Li, L.; Zhao, H.; Wang, J.; Wang, R. Facile Fabrication of Ultrafine Palladium Nanoparticles with Size- and Location-Control in Click-Based Porous Organic Polymers. *ACS Nano* **2014**, *8*, 5352−5364.

(44) Vasimalai, N.; Fernández-Argüelles, M. T.; Espiña, B. Detection of Sulfide Using Mercapto Tetrazine-Protected Fluorescent Gold Nanodots: Preparation of Paper-Based Testing Kit for On-Site Monitoring. *ACS Appl. Mater. Interfaces* **2018**, *10*, 1634−1645.

(45) Vinu, A. Two-Dimensional Hexagonally-Ordered Mesoporous Carbon Nitrides with Tunable Pore Diameter, Surface Area and Nitrogen Content. *Adv. Funct. Mater.* **2008**, *18*, 816−827.

(46) Lhoest, J.-B.; Bertrand, P.; Weng, L. T.; Dewez, J.-L. Combined Time-of-Flight Secondary Ion Mass Spectrometry and X-ray Photoelectron Spectroscopy Study of the Surface Segregation of Poly-(methyl methacrylate) (PMMA) in Bisphenol A Polycarbonate/ PMMA Blends. *Macromolecules* **1995**, *28*, 4631−4637.

(47) Bulusheva, L. G.; Okotrub, A. V.; Flahaut, E.; Asanov, I. P.; Gevko, P. N.; Koroteev, V. O.; Fedoseeva, Y. V.; Yaya, A.; Ewels, C. P. Bromination of Double-Walled Carbon Nanotubes. *Chem. Mater.* **2012**, *24*, 2708−2715.

(48) Lin, S.; Lin, C.-W.; Jhang, J.-H.; Hung, W.-H. Electrodeposition of Long-Chain Alkylaryl Layers on Au Surfaces. *J. Phys. Chem. C* **2012**, *116*, 17048−17054.

(49) Wepasnick, K. A.; Smith, B. A.; Schrote, K. E.; Wilson, H. K.; Diegelmann, S. R.; Fairbrother, D. H. Surface and structural characterization of multi-walled carbon nanotubes following different oxidative treatments. *Carbon* **2011**, *49*, 24−36.

(50) Qu, L.; Liu, Y.; Baek, J.-B.; Dai, L. Nitrogen-Doped Graphene as Efficient Metal-Free Electrocatalyst for Oxygen Reduction in Fuel Cells. *ACS Nano* **2010**, *4*, 1321−1326.

(51) Xiang, Z.; Cao, D.; Huang, L.; Shui, J.; Wang, M.; Dai, L. Nitrogen-Doped Holey Graphitic Carbon from 2D Covalent Organic Polymers for Oxygen Reduction. *Adv. Mater.* **2014**, *26*, 3315−3320.

(52) Spencer, G. H.; Cross, P. C.; Wiberg, K. B. s-Tetrazine. II. Infrared Spectra. *J. Chem. Phys.* **1961**, *35*, 1939−1945.

(53) Kumar, P.; Vahidzadeh, E.; Thakur, U. K.; Kar, P.; Alam, K. M.; Goswami, A.; Mahdi, N.; Cui, K.; Bernard, G. M.; Michaelis, V. K.; Shankar, K. C$_3$N$_5$: A Low Bandgap Semiconductor Containing an Azo-Linked Carbon Nitride Framework for Photocatalytic, Photovoltaic and Adsorbent Applications. *J. Am. Chem. Soc.* **2019**, *141*, 5415−5436.

(54) Liu, Y.; Su, Y.; Guan, J.; Cao, J.; Zhang, R.; He, M.; Gao, K.; Zhou, L.; Jiang, Z. 2D Heterostructure Membranes with Sunlight-Driven Self-Cleaning Ability for Highly Efficient Oil−Water Separation. *Adv. Funct. Mater.* **2018**, *28*, 1706545.

(55) Zine, R.; Sinha, M. Nanofibrous Poly(3-hydroxybutyrate-co-3-hydroxyvalerate)/collagen/graphene Oxide Scaffolds for Wound Coverage. *Mater. Sci. Eng., C* **2017**, *80*, 129−134.

(56) Liu, X.; Wang, Y.; Ju, H.; Yang, F.; Zhang, L.; Luo, X. Micro-mesoporous Divinyl Benzene-based Polymer for Ultrafast, Effective and Selective Removal of Cationic Dyes. *Mater. Chem. Phys.* **2020**, *255*, 123564.

(57) Cychosz, K. A.; Guillet-Nicolas, R.; García-Martínez, J.; Thommes, M. Recent Advances in the Textural Characterization of Hierarchically Structured Nanoporous Materials. *Chem. Soc. Rev.* **2017**, *46*, 389−414.

(58) Comotti, A.; Castiglioni, F.; Bracco, S.; Perego, J.; Pedrini, A.; Negroni, M.; Sozzani, P. Fluorinated Porous Organic Frameworks for Improved CO$_2$ and CH$_4$ Capture. *Chem. Commun.* **2019**, *55*, 8999−9002.

(59) Bracco, S.; Piga, D.; Bassanetti, I.; Perego, J.; Comotti, A.; Sozzani, P. Porous 3D Polymers for High Pressure Methane Storage and Carbon Dioxide Capture. *J. Mater. Chem A* **2017**, *5*, 10328−10337.

(60) Polezhaev, A. V.; Maciulis, N. A.; Chen, C.-H.; Pink, M.; Lord, R. L.; Caulton, K. G. Tetrazine Assists Reduction of Water by Phosphines: Application in the Mitsunobu Reaction. *Chem. - Eur. J.* **2016**, *22*, 13985−13998.

(61) Infantes, L.; Mahon, M. F.; Male, L.; Raithby, P. R.; Teat, S. J.; Sauer, J.; Jagerovic, N.; Elguero, J.; Motherwell, S. 1,2,4,5-Tetrazines vs. Carboxylic Acid Dimers: Molecular Chemistry vs. Supramolecular Chemistry. *Helv. Chim. Acta* **2003**, *86*, 1205−1221.

(62) Schaich, K. M. EPR Methods for Studying Free Radicals in Foods. *Free Radicals in Food*; American Chemical Society, 2002; Chapter 2, pp 12−34.

(63) Yuasa, J.; Fukuzumi, S. Mechanistic Borderline between One-Step Hydrogen Transfer and Sequential Transfers of Electron and Proton in Reactions of NADH Analogues with Triplet Excited States of Tetrazines and Ru(bpy)$_3$$^{2+}$*. *J. Am. Chem. Soc.* **2006**, *128*, 14281−14292.

(64) Benson, C. R.; Fatila, E. M.; Lee, S.; Marzo, M. G.; Pink, M.; Mills, M. B.; Preuss, K. E.; Flood, A. H. Extreme Stabilization and Redox Switching of Organic Anions and Radical Anions by Large-Cavity, CH Hydrogen-Bonding Cyanostar Macrocycles. *J. Am. Chem. Soc.* **2016**, *138*, 15057−15065.